Int. J. Multiphase Flow Vol. 10, No. 3, pp. 249–272, 1984
Printed in Great Britain.

0301-9322/84 $3.00 + .00
Pergamon/Elsevier

MEASUREMENT OF VIRTUAL MASS AND DRAG COEFFICIENTS OF A DISK OSCILLATING SINUSOIDALLY IN A TWO-PHASE MIXTURE

P. S. KAMATH
Creare R & D, Inc., Hanover, New Hampshire, U.S.A.

and

R. T. LAHEY, JR. and D. R. HARRIS
Department of Nuclear Engineering, Rensselaer Polytechnic Institute, Troy, NY 12181, U.S.A.

(*Received* 17 *March* 1982; *in revised form* 7 *July* 1983)

Abstract—This paper presents an experimental determination of the virtual mass and drag coefficients of a disk oscillating sinusoidally in a two-phase mixture of air flowing through stagnant water. The purpose of this experiment was to determine the importance of virtual mass on the transient response of an INEL-type drag-disk flow meter.

The results indicate that for a given void fraction, the virtual mass coefficient increases, and the drag coefficient decreases, with increasing amplitude parameter. Also, for a given amplitude parameter, the virtual mass coefficient decreases, and the drag coefficient increases, with increasing void fraction.

Based on the measured virtual mass coefficients, it was concluded that when an INEL-type drag-disk is used for the measurement of transient two-phase flows, virtual mass effects may be neglected in the analysis of its response without appreciable error.

1. INTRODUCTION

In transient single-phase flows, the net hydrodynamic force on a bluff body is usually expressed as the sum of the virtual mass and drag forces (Morrison 1950). Analytical expressions for these forces have been previously obtained (Lyle & Lai 1972; Lai 1973) for low Reynolds number (i.e. Stokes) flows, in which there is no separation in the wake. Prior experimental work has centered around the determination of the Fourier-averaged drag and virtual mass coefficients, C_D and C_M, as functions of the period parameter. Experiments have been conducted for single-phase sinusoidally oscillating liquid flows past cylinders (Keulegan & Carpenter 1958; Sarpkaya 1975), spheres (Sarpkya 1975), and plates (Keulegan & Carpenter 1958). Mercier (1973) oscillated a cylinder in a low speed stream and the C_M and C_D thus obtained were found to be in good agreement with those previously obtained by Keulegan & Carpenter (1958), for a stationary cylinder in an oscillating liquid flow.

Here we present an experimental determination of the virtual mass and drag coefficients for a disk oscillating sinusoidally in a two-phase mixture of air flowing through stagnant water. The primary purpose of the experiment was to assess the importance of the effect of the virtual mass of the disk on the transient response of an INEL-type drag-disk during a blowdown transient. In our experiment, the disk was oscillated in a two-phase mixture, although for an actual drag-disk, both the disk and the fluid undergo acceleration.

Thus, according to potential flow theory, the virtual mass coefficient determined from our experiment should be smaller than in the case of an actual drag-disk. However, the effect of viscosity can be expected to compensate for this difference to some extent.

2. DISCUSSION OF EXPERIMENT

The apparatus used in this experiment is shown schematically in figure 1. The disk was 5.08 cm (2 in.) in diameter, and was made of 304 stainless steel. It was sinusoidally oscillated by an electromechanical seismic shaker in a two-phase mixture of air flowing upward through a vertical plexiglass tube containing stagnant water. Figure 2 is a picture of the apparatus at a low air flow rate.

The experimental conditions were such that the system pressure drop was dominated

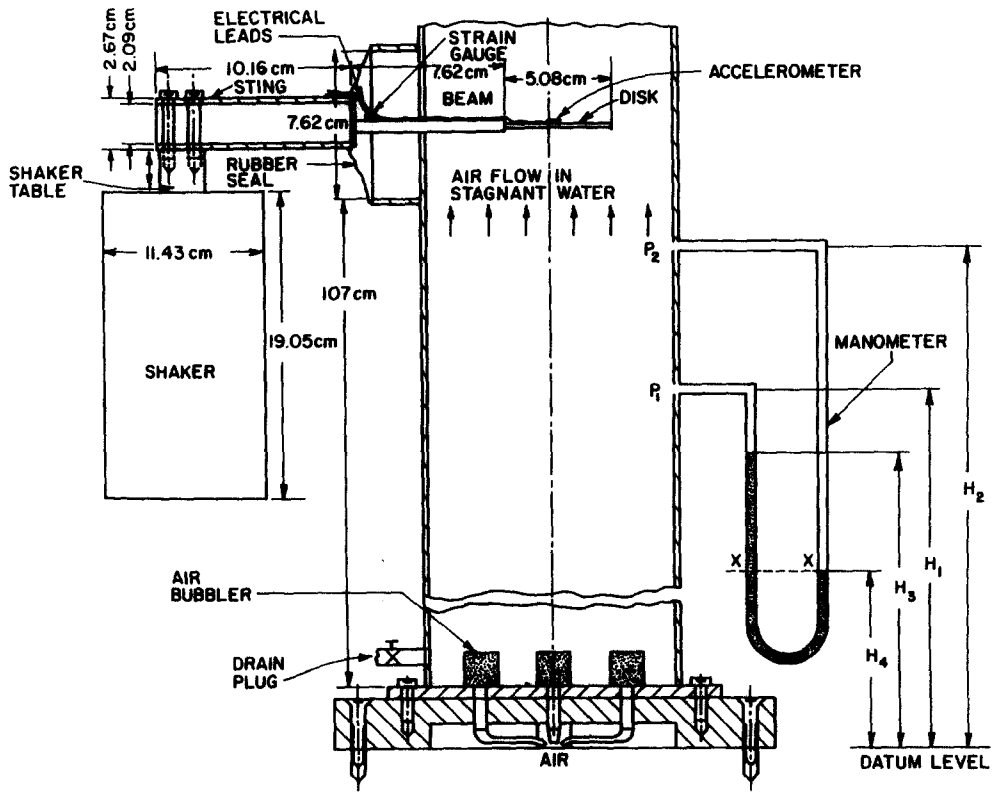

Figure 1. Experimental setup for the measurement of virtual mass and drag coefficients.

by the hydrostatic head; thus the global void fraction, $\langle\alpha\rangle$, of the two-phase mixture could be measured using a manometer. An accelerometer mounted on the disk measured the instantaneous acceleration of the disk, and a strain-gauge mounted on the beam measured the instantaneous sum of the drag and inertia forces. The shaker, shown in figure 2, was of the electromechanical type, and employed special air bearings to ensure sufficient lateral stiffness. It was driven by a power amplifier, the input to which was a sinusoidal signal of the desired frequency from a function generator.

The beam, which supported the disk, was also made of 304 stainless steel and was of rectangular cross-section. It was designed to be flexible enough to give a measurable strain, and yet stiff enough to prevent contamination of the strain gauge and accelerometer signals by its modal frequencies. To insure this, the natural frequency of the beam, f_n, given by,

$$f_n = \frac{k}{M} = \frac{3EI}{Ml^3}, \qquad [1]$$

where k is the beam stiffness, was made greater than four times the highest frequency of oscillation of the disk. In [1], E is Young's modulus and I, the moment of inertia about the neutral axis. The cantilever arm length, l, was taken to be the length of the beam (figure 1). The mass, M (132 gm), at the outer end of the cantilever was calculated as an equivalent mass, concentrated at the center of the disk, of the distributed beam and disk masses.

The beam strain at the location of the strain gauge equals the stress divided by Young's modulus, or,

$$\text{Strain} = \frac{F_{SG}Lh}{2EI} \qquad [2]$$

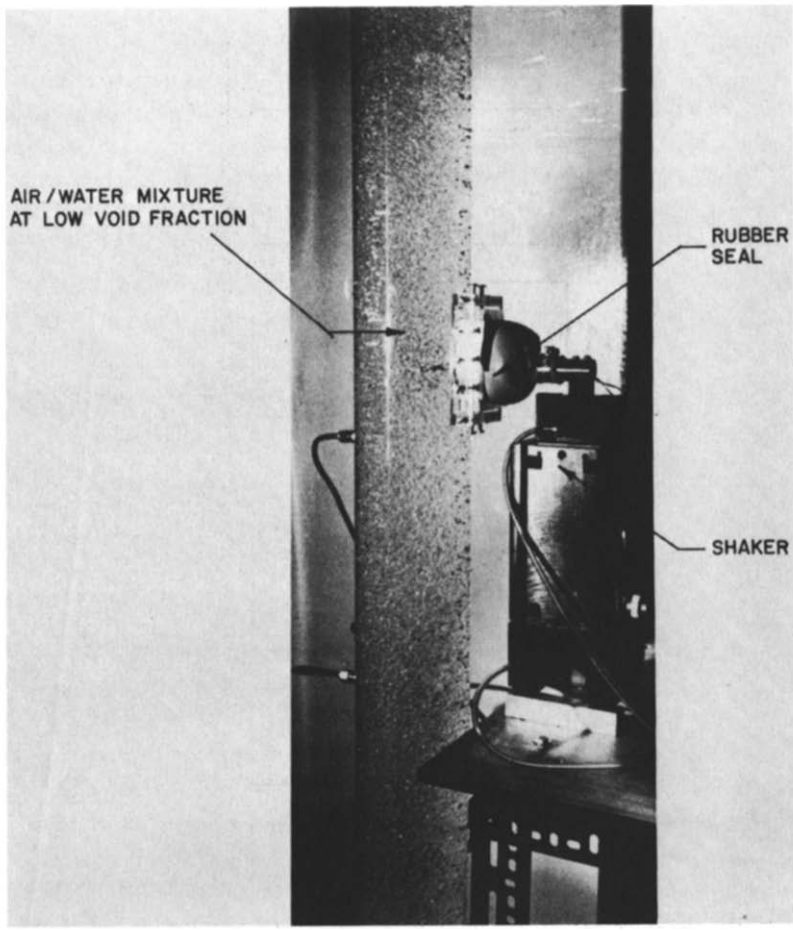

Figure 2. Experimental setup with air/water mixture at low void fraction.

where the thickness of the beam, h, was 0.17 cm (0.066 in.), its breadth was 0.51 cm (0.2 in.) and L, its length, was 7.62 cm (3 in.). To size the strain gauge, the force at the location of the strain gauge, F_{SG}, was estimated using [9], presented later with typical values for the virtual mass (C_M) and drag coefficients (C_D), given by Keulegan & Carpenter (1958).

The beam was welded onto a 304 stainless steel sting, which was made stiff enough to give zero-slope and zero-deflection conditions at the fixed end of the beam.

Figure 3 shows a block diagram of the data acquisition electronics used in the experiment. The signals from the accelerometer and the strain gauge were amplified to a range of 0 to 10 volts to be compatible with the analog-to-digital (A/D) converter. An active low-pass filter with a cutoff frequency of 100 Hz was used to filter out higher frequency noise from the signals. The signals were then sampled and digitized. Table 1 shows the sampling frequencies for the various frequencies of oscillation. A 60 Hz noise in the strain gauge signal necessitated a sampling frequency above the Nyquist value of 120 Hz for all cases. The digital signals were fed into a PDP-9 mini-computer through a CAMAC module and stored on digital tape. Before processing the data, the strain guage and accelerometer signals were smoothed using a numerical low-pass filter with a linear roll-off (Ormsby 1971). The procedure used is fully described by Kamath & Lahey (1981). Table 1 shows the sampling frequencies (f_s), and the filter cut-off frequencies (f_T) for the various forcing frequencies (f_0) investigated.

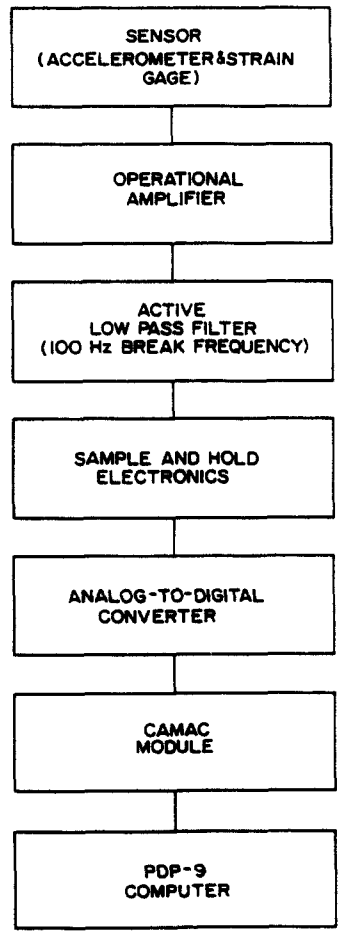

Figure 3. Block diagram of data acquisition electronics.

To calibrate to strain gauge, the paddle was mounted on a rigid support and the disk was loaded with known weights. As expected, the force was observed to have a linear relationship with strain gauge output. The accelerometer was then calibrated by oscillating the paddle in air. The inertia force measured by the strain gauge and the known mass of the disk and beam were used to calculate the acceleration at each instant of time, which was then compared to the output of the accelerometer to obtain a calibration constant.

Table 1. Sampling frequencies and lowpass filter cutoff and roll-off termination frequencies for different forcing frequencies

Frequency of Oscillation (f_o)	Sampling Frequency (f_s)	Cutoff frequency of Numerical Filter (f_c)	Roll-off Termination Frequency of Numerical Filter (f_T)
31.25 Hz	500 Hz	40 Hz	44 Hz
15.625 Hz	250 Hz	20 Hz	22 Hz
7.8125 Hz	125 Hz	10 Hz	11 Hz
3.90625 Hz	125 Hz	5 Hz	6 Hz
1.953125 Hz	125 Hz	2.5 Hz	3.5 Hz

3. DISCUSSION OF ANALYSIS

The equation of motion of the isolated body, consisting of the disk and the beam, is given by Newton's second law of motion,

$$\begin{bmatrix}\text{time rate of change}\\ \text{of momentum of the}\\ \text{isolated body}\end{bmatrix} = \begin{bmatrix}\text{sum of the external}\\ \text{forces on the}\\ \text{isolated body}\end{bmatrix} \quad [3]$$

The left-hand side of [3] is given by,

$$\begin{bmatrix}\text{time rate of change}\\ \text{of momentum of the}\\ \text{isolated body}\end{bmatrix} = \frac{M}{g_c}\frac{d^2x}{dt^2} \equiv \frac{M}{g_c}\ddot{x} \quad [4]$$

where x is the displacement.

The external forces consist of the drag and virtual mass forces in addition to the shear force at the location of the strain gauge, F_{SG}. Since the vapor phase drag was relatively unimportant in our low pressure experiment, only the liquid phase drag was included in our model. Hence, the expression used for the drag force was,

$$F_d \triangleq \frac{C_D}{2g_c}\left(\frac{\pi D^2}{4}\right)[\rho_l\langle 1-\alpha\rangle\langle v_l-\dot{x}\rangle\langle|v_l-\dot{x}|\rangle], \quad [5]$$

where C_D is the drag coefficient and D is the disk diameter. The one-dimensional liquid phase velocity, $\langle v_l\rangle$, is zero in this experiment.

The virtual mass force was expressed as,

$$F_{vm} \triangleq \frac{C_m\langle\bar{\rho}\rangle}{g_c}\left(\frac{D^3}{3}\right)\frac{d}{dt}[U_m-\dot{x}] \quad [6]$$

where C_m is the virtual mass coefficient and $\langle\bar{\rho}\rangle$ is the two-phase density. The representative velocity of the two-phase mixture is the center-of-mass velocity, U_m, given by,

$$U_m \triangleq \frac{G}{\langle\bar{\rho}\rangle} = \frac{[\rho_L\langle 1-\alpha\rangle\langle v_L\rangle + \rho_G\langle\alpha\rangle\langle v_G\rangle]}{(\rho_L\langle 1-\alpha\rangle + \rho_G\langle\alpha\rangle)}. \quad [7]$$

Since the motion of the fluid is steady, $(dU_m/dt) = 0$; thus [6] becomes,

$$F_{vm} = -\frac{C_m\langle\bar{\rho}\rangle D^3\ddot{x}}{3g_c}. \quad [8]$$

Substituting [4], [5] and [8] into [3], including the shear force, F_{SG}, and rearranging, the resultant equation is:

$$F_{SG} = \left[M + C_m\left(\frac{D^3}{3}\right)\langle\bar{\rho}\rangle\right]\ddot{x} + \frac{C_D}{2}\frac{\pi D^2}{4}[\rho_L\langle 1-\alpha\rangle\dot{x}|\dot{x}|]. \quad [9]$$

The expression forms the basis of the calculation of the coefficients C_m and C_D from the measurement of F_{SG} and $\ddot{x}$. The data reduction technique employed will be described in the next section.

4. DATA REDUCTION

The virtual mass and drag coefficients, C_m and C_D, appear in the virtual mass and drag components of the total force given in [9].

The virtual mass force, being an inertial force, is in-phase with the acceleration. Also, it will be shown shortly that for sinusoidal motion of the disk, the Fourier series for drag force has frequency components that are odd multiples of the fundamental frequency (Keulegan & Carpenter 1958). In this series, the component with the largest magnitude and the lowest frequency (i.e. the fundamental) is one-quarter cycle out-of-phase with the acceleration. Thus a Finite Fourier Transform of the force signal, $F_{SG}(t)$, can be used to extract the Fourier-averaged drag and inertial components of the total force. This approach has been followed previously by Keulegan & Carpenter (1958). Garrison *et al.* (1977), used a least-squares approach which, for sinusoidal motion of the body yields a C_m identical to that of Keulegan and Carpenter, but a C_D that is somewhat different. Both methods, though theoretically sound, were found unsuitable for use in this experiment. These methods, have been evaluated in detail elsewhere (Kamath & Lahey 1981) and will not be discussed further here.

The method used in the present study uses the acceleration signal, $\ddot{x}(t)$, as the kernel to extract the inertial and drag components of the force signal.

To use this approach, [9] is multiplied by $\ddot{x}(t)$ and integrated over an integral number of cycles. That is,

$$\int_t^{t+nT} F_{SG}(t)\ddot{x}(t)\,dt = \left[M + C_m\left(\frac{D^3}{3}\right)\langle\bar{\rho}\rangle\right]\int_t^{t+nT}[\ddot{x}(t)]^2\,dt + \frac{C_D}{2}\left(\frac{\pi D^2}{4}\right)\left[\rho_L\langle 1-\alpha\rangle\int_t^{t+nT}\dot{x}|\dot{x}|\ddot{x}\,dt\right]. \quad [10]$$

Equation [9] is then multiplied by $\ddot{x}(t + T/4)$ and again integrated over the same time interval,

$$\int_t^{t+nT} F_{SG}(t)\ddot{x}(t+T/4)\,dt = \left[M + C_m\left(\frac{D^3}{3}\right)\langle\bar{\rho}\rangle\right]\int_t^{t+nT}\ddot{x}(t)\ddot{x}(t+T/4)\,dt + \frac{C_D}{2g_c}\left(\frac{\pi D^2}{4}\right)\left[\rho_L\langle 1-\alpha\rangle\int_t^{t+nT}\dot{x}|\dot{x}|\ddot{x}(t+T/4)\,dt\right]. \quad [11]$$

Let us now define:

$$I_1 \triangleq \int_t^{t+nT} F_{SG}(t)\ddot{x}(t)\,dt, \quad [12]$$

$$I_2 \triangleq \int_t^{t+nT} F_{SG}(t)\ddot{x}(t+T/4)\,dt, \quad [13]$$

$$I_3 \triangleq \int_t^{t+nT}[\ddot{x}(t)]^2\,dt, \quad [14]$$

$$I_4 \triangleq \int_t^{t+nT}\ddot{x}(t+T/4)\ddot{x}(t)\,dt, \quad [15]$$

$$I_5 \triangleq \int_t^{t+nT}\dot{x}(t)|\dot{x}(t)|\ddot{x}(t)\,dt, \quad [16]$$

$$I_6 \triangleq \int_t^{t+nT} \dot{x}(t)|\dot{x}(t)|\ddot{x}(t + T/4)\,dt, \quad [17]$$

$$A_1 \triangleq \left[M + C_m\left(\frac{D^3}{3}\right)\langle\bar{\rho}\rangle \right], \quad [18]$$

and,

$$A_2 \triangleq \frac{C_D}{2}\left(\frac{\pi D^2}{4}\right)\rho_l\langle 1 - \alpha\rangle. \quad [19]$$

In terms of these variables, [10] and [11] reduce to,

$$I_1 = A_1 I_3 + A_2 I_5, \quad [20]$$

$$I_2 = A_1 I_4 + A_2 I_6. \quad [21]$$

Solving [20] and [21] for A_1,

$$A_1 = \frac{I_1 I_6 - I_2 I_5}{I_3 I_6 - I_4 I_5}, \quad [22]$$

and A_2,

$$A_2 = \frac{I_3 I_2 - I_4 I_1}{I_3 I_6 - I_4 I_5}. \quad [23]$$

Now substituting [22] and [23] into [18] and [19] and solving for the coefficients C_m and C_D, one obtains,

$$C_m = \left[\frac{I_1 I_6 - I_2 I_5}{I_3 I_6 - I_4 I_5} - M\right]\frac{3}{\langle\bar{\rho}\rangle D^3}, \quad [24]$$

and,

$$C_D = \frac{8}{\pi D^2 \rho_L\langle 1 - \alpha\rangle}\left\{\frac{I_3 I_2 - I_4 I_1}{I_3 I_6 - I_4 I_5}\right\}. \quad [25]$$

For sinusoidal motion of the disk, the displacement, velocity and acceleration are given by,

$$x(t) = x_0 \sin 2\pi f_0 t \quad [26]$$

$$\dot{x}(t) = x_0(2\pi f_0)\cos 2\pi f_0 t \quad [27]$$

and,

$$\ddot{x}(t) = -x_0(2\pi f_0)^2 \sin 2\pi f_0 t. \quad [28]$$

The product, $\dot{x}|\dot{x}|$ can be expanded in a Fourier Series as,

$$\dot{x}|\dot{x}| = x_0(2\pi f_0)^2 \sum_{n=\text{odd}} (-1)^{(n+1)/2}\frac{8}{n(n^2-4)\pi}\cos(2\pi n f_0 t). \quad [29]$$

Also, the acceleration, shifted in phase by one-quarter cycle, is given by,

$$\ddot{x}(t + T/4) = -x_0(2\pi f_0)^2 \cos 2\pi f_0 t. \quad [30]$$

Thus, the integrals, I_4 and I_5, given by [15] and [16], are equal to zero due to orthogonality. Also, the product, $\dot{x}|\dot{x}|$, in [17] for I_6 can be eliminated using [29] and noting that there is only one non-zero term in the series, thus,

$$I_6 = \int_t^{t+nT} x_0^2(2\pi f_0)^2 \frac{8}{3\pi} \cos 2\pi f_0 t(-x_0)(2\pi f_0)^2 \cos 2\pi f_0 t \, dt, \quad [31]$$

where [28] has been used for the acceleration, $\ddot{x}$. Using [30], [31] can be expressed as,

$$I_6 = -\frac{8}{3\pi} x_0 \int_t^{t+nT} [\ddot{x}(t + T/4)]^2 \, dt. \quad [32]$$

Thus noting that $I_4 = I_5 = 0$ for sinusoidal motion of the disk, and using [12]–[14] and [32] for I_1, I_2, I_3 and I_6, [24] and [25] can be written in explicit form as,

$$C_m = \left[\frac{g_c \int_t^{t+nT} F_{SG}(t)\ddot{x}(t) \, dt}{\int_t^{t+nT} [\ddot{x}(t)]^2 \, dt} - M \right] \frac{3}{D^3 \langle \bar{\rho} \rangle}, \quad [33]$$

and,

$$C_D = \left[\frac{\int_t^{t+nT} F_{SG}(t)\ddot{x}(t + T/4) \, dt}{\int_t^{t+nT} [\ddot{x}(t + T/4)]^2 \, dt} \right] \frac{3g_c}{\rho_f \langle 1 - \alpha \rangle D^2 x_0}. \quad [34]$$

Equations [33] and [34] were used to calculate the coefficients, C_m and C_D.

The amplitude of oscillation of the disk, x_0, was calculated by using the acceleration signal, $\ddot{x}(t)$. Assuming sinusoidal motion of the disk, the recorded acceleration signal is approximated by a chopped sinusoid, represented by,

$$\ddot{x}(t) = \begin{cases} A_0 \sin 2\pi f_0 t, & |t| \le T_0 \\ 0, & \text{otherwise} \end{cases} \quad [35]$$

where, according to [28],

$$A_0 \triangleq -x_0(2\pi f_0)^2. \quad [36]$$

If Δt is the time interval between samples, and N is the number of samples, then,

$$T_0 = \frac{N\Delta t}{2} \quad [37]$$

Let us now take the Fourier Transform of [35],

$$\bar{\ddot{x}}(f) \triangleq \int_{-\infty}^{\infty} \ddot{x}(t) \, e^{-j2\pi ft} \, dt, \quad [38]$$

and the inverse transformation is,

$$\ddot{x}(t) \triangleq \int_{-\infty}^{\infty} \bar{\ddot{x}}(f)\, e^{j2\pi ft}\, df. \tag{39}$$

Substituting [35] into [36] and integrating one obtains,

$$\bar{\ddot{x}}(f) = -jA_0T_0, \tag{40}$$

and,

$$|\bar{\ddot{x}}(f_0)| = |A_0|T_0. \tag{41}$$

Substituting [36] and [37] into [41], and solving for x_0, one obtains,

$$x_0 = \frac{2|\bar{\ddot{x}}(f_0)|}{(2\pi f_0)^2 N\Delta t}. \tag{42}$$

This expression was used for calculation of x_0. The Fourier transform calculations, for the evaluation of $\bar{\ddot{x}}(f_0)$, were performed using a Fast Fourier Transform (FTT) algorithm proposed by Brigham (1974). The frequency of oscillation, f_0, was determined from the location of the peak of the power spectral density (PSD) function of the acceleration signal, given by,

$$\text{PSD} \triangleq [\bar{\ddot{x}}(f)\bar{\ddot{x}}^*(f)]^{1/2}, \tag{43}$$

where $\bar{\ddot{x}}(f)^*$ is the complex conjugate $\bar{\ddot{x}}(f)$. The calculated value of x_0 was used in [33] and [34] for the calculation of C_m and C_D.

5. EXPERIMENTAL RESULTS

The measured virtual mass and drag coefficients are listed in tables 2–7 for various void fractions. The results are tabulated for a range of amplitude parameters between about 1/10 and 4/3, the range expected for an INEL drag-disk undergoing a blowdown transient. The Reynolds numbers in these tables were calculated using,

$$\text{Re} \triangleq \frac{\langle \bar{\rho} \rangle u_0 D}{\mu_{2\phi}} \tag{44}$$

where the two-phase density and dynamic viscosity properties are defined as,

$$\langle \bar{\rho} \rangle \triangleq \rho_L - (\rho_L - \rho_G)\langle \alpha \rangle \tag{45}$$

$$\mu_{2\phi} \triangleq \mu_L - (\mu_L - \mu_G)\langle \alpha \rangle \tag{46}$$

and u_0, the maximum sinusoidal velocity, given by,

$$u_0 = x_0(2\pi f_0). \tag{47}$$

Substituting [45]–[47] into [44] the Reynolds number can be written as,

$$\text{Re} = f(\alpha)x_0D(2\pi f_0), \tag{48}$$

Table 2. Virtual mass and drag coefficients at various amplitude parameters for single-phase liquid ($\langle\alpha\rangle = 0$)

Amplitude Parameter $\left(\frac{2\pi x_o}{D}\right)$	Virtual Mass Coefficient (C_m)	Drag Coefficient (C_D)	Reynolds Number
0.10	0.27	19.70	1,934
0.14	0.58	15.60	3,406
0.20	0.52	14.10	1,716
0.20	0.48	15.30	1,808
0.26	0.62	12.66	6,134
0.30	0.42	10.13	7,125
0.33	1.21	12.10	3,922
0.37	0.79	6.73	4,305
0.43	1.24	9.63	4,912
0.49	1.04	3.65	5,792
0.51	1.09	5.38	6,075
0.66	1.93	3.54	3,929
0.91	1.20	4.51	5,368
0.91	1.68	7.88	5,524
0.92	1.57	11.38	5,755
0.94	1.59	3.64	5,556
1.22	1.83	5.07	7,216

where,

$$f(\alpha) \triangleq \frac{(\rho_L - [\rho_L - \rho_G]\langle\alpha\rangle}{\mu_L - (\mu_L - \mu_v)\langle\alpha\rangle}. \qquad [49]$$

Equations [48] and [49] were used for the calculation of the Reynolds numbers listed in tables 2–7. Typical accelerometer and strain gauge signals, at frequencies (f) of 15.6 Hz, 7.8 Hz and 1.9 Hz, are shown in figures 4, 6 and 8. Before reducing the data, they were smoothed using the numerical low-pass filter algorithm mentioned previously. The corresponding

Table 3. Virtual mass and drag coefficients at various amplitude parameters for a void fraction of 3.5%

Amplitude Parameter $\left(\frac{2\pi x_o}{D}\right)$	Virtual Mass Coefficient (C_m)	Drag Coefficient (C_D)	Reynolds Number
0.12	0.50	31.94	2,850
0.14	0.47	28.35	3,289
0.21	0.41	16.13	4,852
0.22	0.24	13.31	5,269
0.33	0.52	16.81	3,950
0.35	0.77	14.12	4,112
0.41	0.81	10.26	4,649
0.49	0.49	5.11	5,751
0.73	0.90	4.29	4,291
0.87	1.17	3.56	5,066
0.91	0.93	2.98	5,413
0.93	0.94	1.75	5,481
0.98	1.01	8.21	5,788
1.15	1.29	4.5	6,810
1.26	0.90	4.03	7,476

Table 4. Virtual mass and drag coefficients at various amplitude parameters for a void fraction of 7%

Amplitude Parameter $(\frac{2\pi x_o}{D})$	Virtual Mass Coefficient (C_m)	Drag Coefficient (C_D)	Reynolds Number
0.11	0.58	34.20	2,501
0.13	0.43	33.04	3,028
0.16	0.45	24.80	3,757
0.18	0.42	21.96	4,236
0.35	0.36	15.25	4,105
0.50	0.73	4.41	5,852
0.74	0.79	12.42	4,367
0.82	1.11	2.82	4,862
0.85	0.95	3.66	5,032
1.06	0.81	1.82	6,266
1.10	1.00	7.16	6,530
1.17	1.26	2.62	6,512

Table 5. Virtual mass and drag coefficients at various amplitude parameters for a void fraction of 12%

Amplitude Parameter $(\frac{2\pi x_o}{D})$	Virtual Mass Coefficient (C_m)	Drag Coefficient	Reynolds Number
0.12	0.29	31.26	2,735
0.14	0.30	23.25	3,171
0.16	0.23	24.00	3,744
0.21	0.25	18.20	4,950
0.36	0.46	16.80	1,380
0.48	0.57	5.83	5,638
0.49	0.48	5.70	5,657
0.82	0.98	6.38	4,829
1.05	0.87	6.64	6,207
1.23	1.21	5.81	7,281

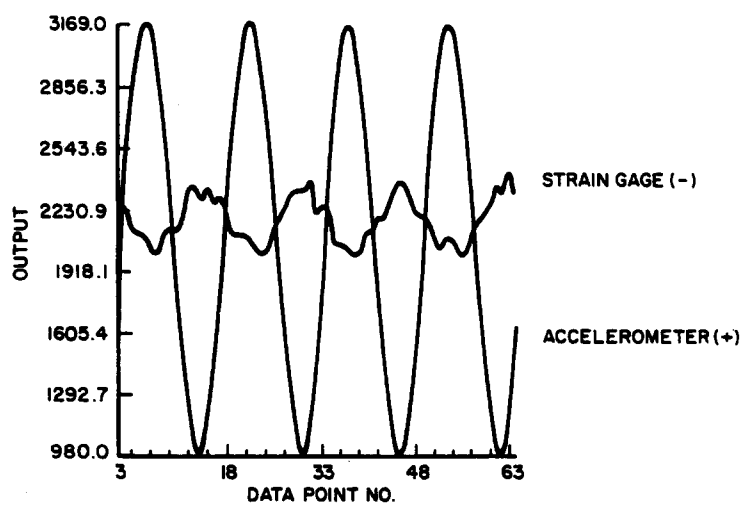

Figure 4. Unfiltered accelerometer and strain gage outputs in single-phase liquid at 15.6 Hz.

Table 6. Virtual mass and drag coefficients at various amplitude parameters for a void fraction of 15.5%

Amplitude Parameter $(\frac{2\pi x_o}{D})$	Virtual Mass Coefficient (C_m)	Drag Coefficient	Reynolds Number
0.12	0.19	25.60	2,879
0.13	0.44	37.30	2,943
0.16	0.38	25.40	3,700
0.20	0.39	22.60	4,638
0.34	0.64	11.60	3,987
0.40	0.84	6.47	1,744
0.46	0.78	10.90	5,408
0.75	0.99	7.04	4,423
0.80	1.09	10.00	1,709
0.91	0.89	4.60	5,379
1.08	0.94	1.70	5,961
1.14	0.96	3.94	6,756
1.18	1.13	2.82	6,967
1.33	0.98	3.44	7,875

filtered signals are shown in figures 5, 7 and 9. In figures 4–9, the strain gauge and accelerometer signals are very nearly inphase,† indicating that inertia forces were dominant.

In figure 4, which is for single-phase liquid and an oscillation frequency of $f_0 = 15.6$ Hz, the accelerometer signal is seen to be very nearly sinusoidal. The strain gauge signal had a 60 Hz noise component. A comparison of figures 4 and 5 shows that the numerical filter effectively removed the 60 Hz noise component.

Figure 6 shows the sampled signals at a frequency of 7.8 Hz and a void fraction of 19%, which was the highest void fraction used in the experiment. At this void fraction, the motion

Table 7. Virtual mass and drag coefficients at various amplitude parameters for a void fraction of 19%

Amplitude Parameter $(\frac{2\pi x_o}{D})$	Virtual Mass Coefficient (C_m)	Drag Coefficient (C_D)	Reynolds Number
0.12	0.15	31.63	2,853
0.14	0.25	21.00	3,296
0.16	0.45	30.75	3,538
0.16	0.33	26.0	3,666
0.26	0.32	9.80	3,093
0.29	0.54	6.74	3,400
0.30	0.30	13.62	3,454
0.31	0.23	15.80	3,631
0.68	0.66	5.00	3,997
0.71	0.82	10.90	4,193
0.73	0.55	7.64	4,307
0.79	0.57	3.28	4,679
0.95	0.67	9.25	5,609
1.18	1.18	4.50	6,963

†Note inversion of polarity of strain gage signal.

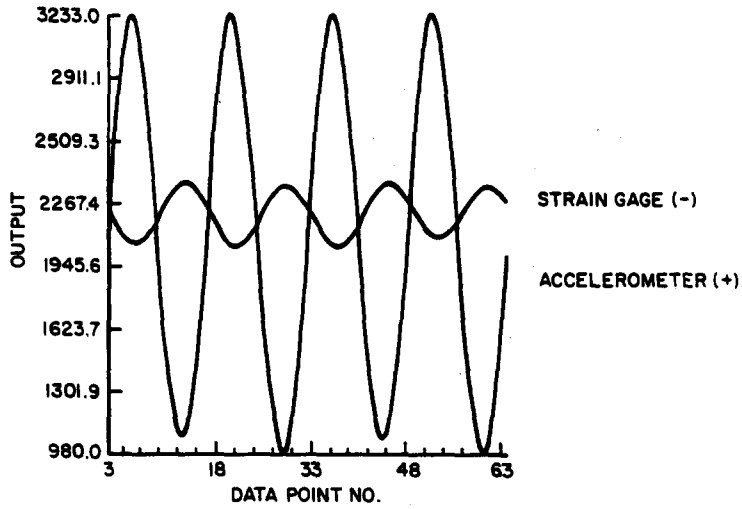

Figure 5. Filtered accelerometer and strain gage outputs in single-phase liquid at 15.6 Hz with a cutoff frequency of 20 Hz.

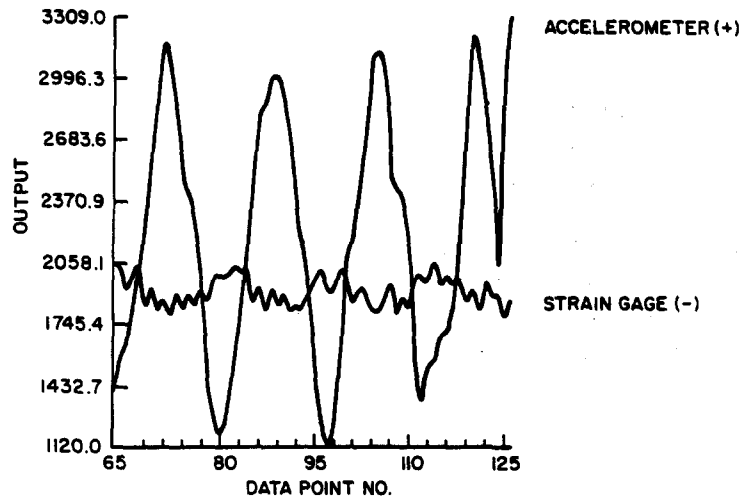

Figure 6. Unfiltered accelerometer and strain gage outputs for a void fraction of 19% at 7.8 Hz.

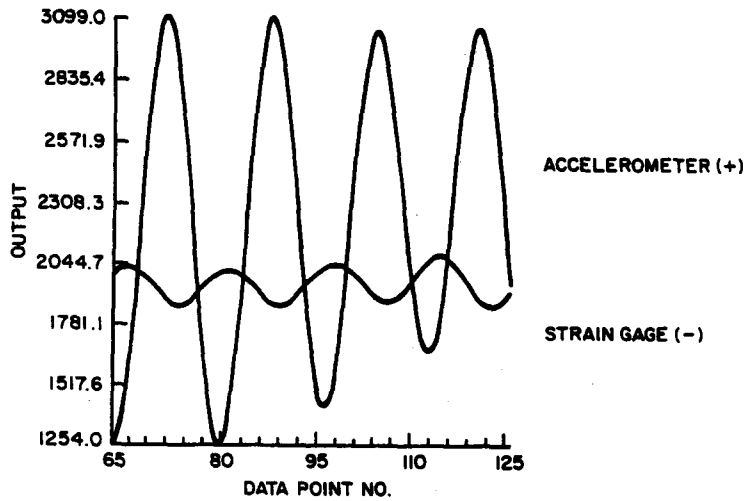

Figure 7. Filtered accelerometer and strain gage outputs for a void fraction of 19% at 7.8 Hz with a cutoff frequency of 10 Hz.

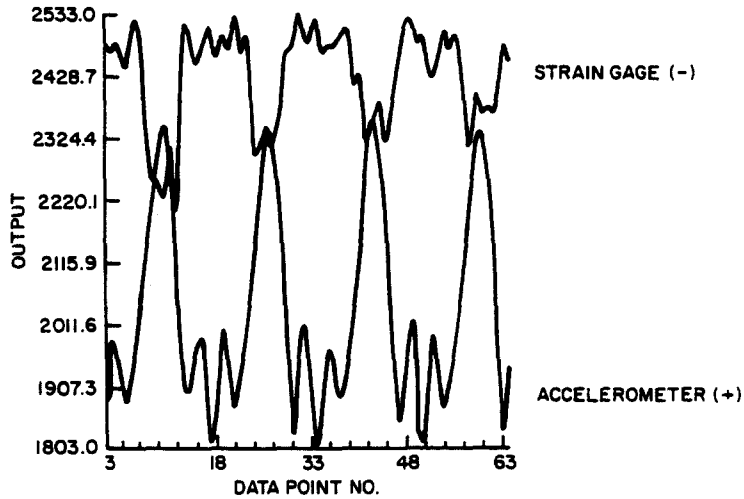

Figure 8. Unfiltered accelerometer and strain gage outputs for single-phase liquid at 1.9 Hz.

of the two-phase fluid included a number of bubble swarms (i.e. eddies), propagating upwards through the pipe. The agitation of the disk due to the eddies was almost periodic. Figures 6 and 7 show that the effect of the bubble swarms on the accelerometer signal was to introduce a low frequency component, whereas the strain gauge is seen to be less sensitive. At lower void fractions, there were no bubble swarms but the disk was perturbed by the effect of bubbles preferentially collecting under the lower surface of the disk, as shown in figure 10.

As can be seen in figure 8, the motion of the paddle at a frequency of 1.9 Hz, though periodic, was not sinusoidal. This was due to the effect of the restraining mechanism on the shaker, which arrested the downward movement of the shaker bar on which the paddle was mounted. However, the filtered versions of these signals, shown in figure 9, which were used to reduce the data, are very nearly sinusoidal.

The virtual mass and drag coefficients in [9] were calculated from the filtered force and acceleration signals using [33] and [34] respectively, and then correlated against the amplitude parameter ($2\pi x_0/D$). Figures 11–22 show the variation of the virtual mass and drag

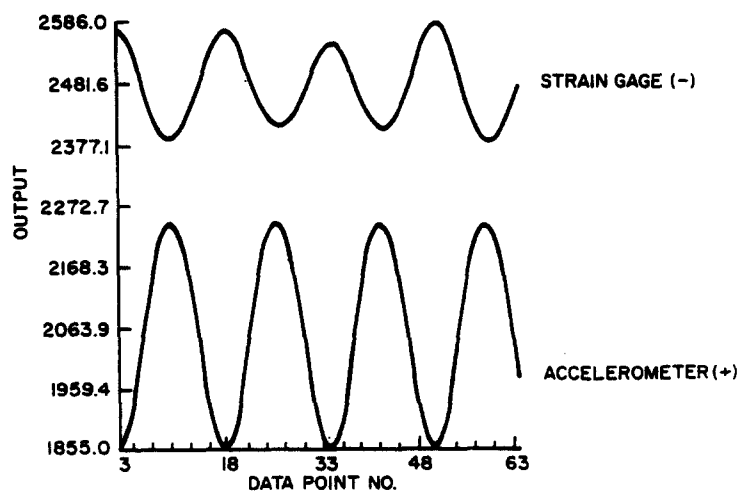

Figure 9. Filtered accelerometer and strain gage outputs for single-phase liquid at 1.9 Hz and a cutoff frequency of 2.5 Hz.

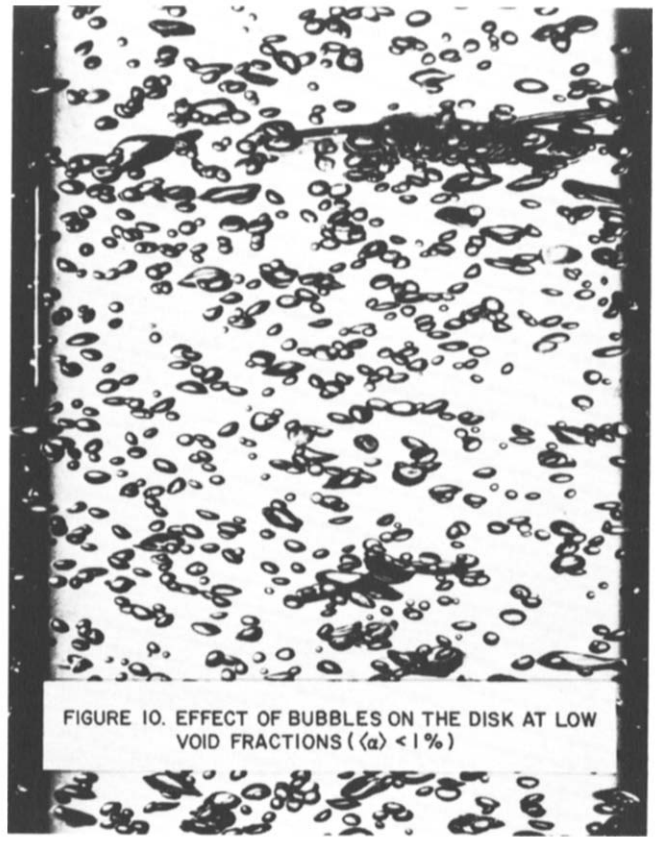

Figure 10.

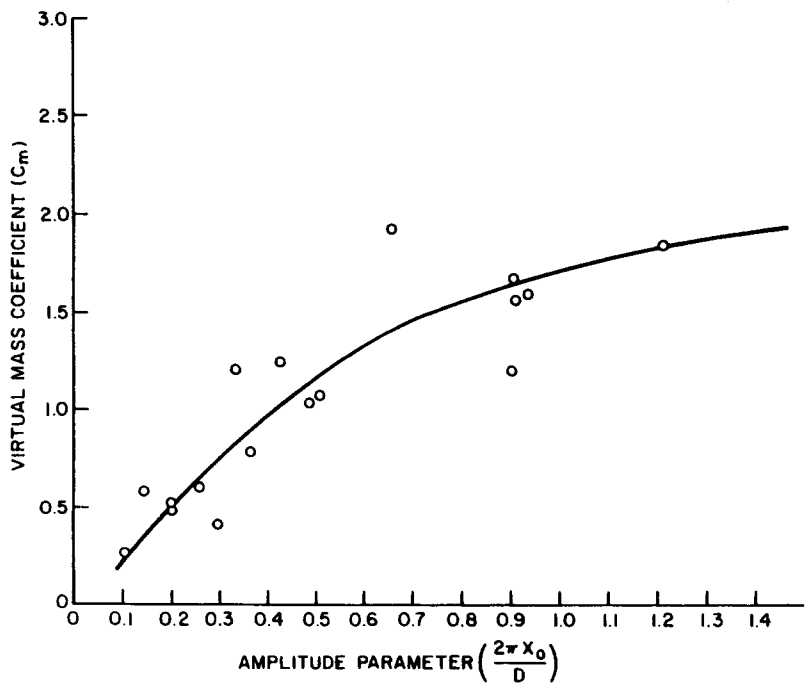

Figure 11. Variation of virtual mass coefficient with amplitude parameter for single-phase liquid ($\langle\alpha\rangle = 0$).

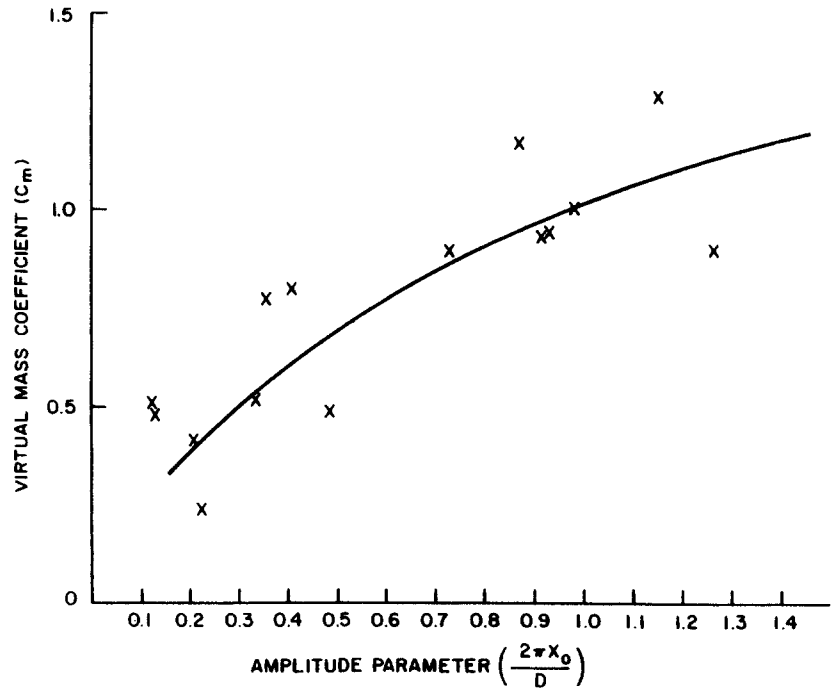

Figure 12. Variation of virtual mass coefficient with amplitude parameter for a void fraction of 3.5%.

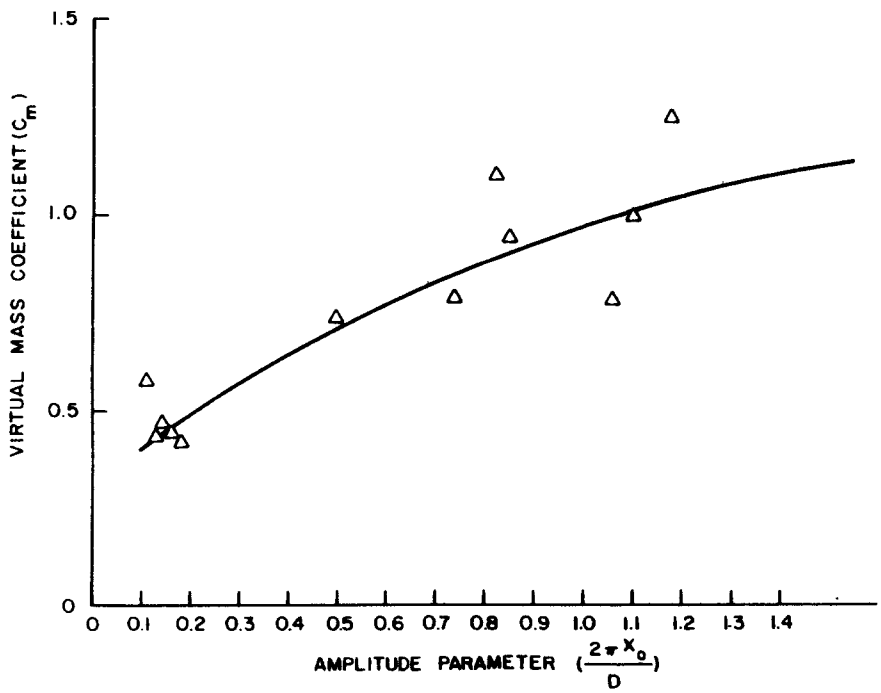

Figure 13. Variation of virtual mass coefficient with amplitude parameter for a void fraction of 7%.

coefficients with amplitude parameter for the various void fractions tested. The best fit lines in these figures show that C_m and C_D vary monotonically with amplitude parameter.The information in figures 11–22 is also presented in tables 2–7.

As seen in figure 11, the virtual mass coefficient for single-phase liquid increases, at a decreasing rate, with amplitude parameter in the measured range. The drag coefficient, as seen in figure 17, decreases rapidly up to an amplitude parameter of 0.5, and then

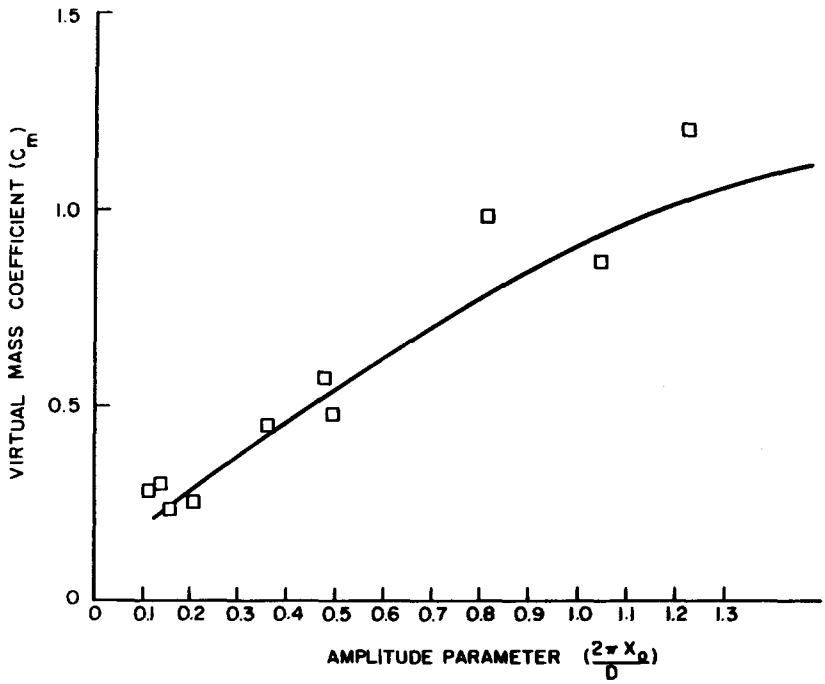

Figure 14. Variation of virtual mass coefficient with amplitude parameter for a void fraction of 12%.

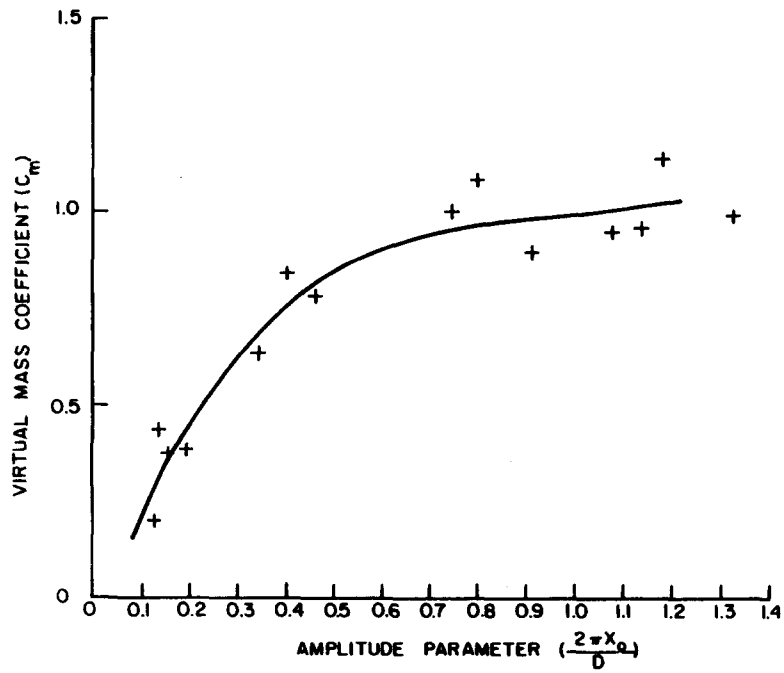

Figure 15. Variation of virtual mass coefficient with amplitude parameter for a void fraction of 15.5%.

decreases at a much slower rate, finally approaching the steady-state value of the drag coefficient, 1.13 (Carmody 1964). Our results are for amplitude parameters generally smaller than those of Keulegan & Carpenter (1958). However, the trends observed in our data are similar to those found by Keulegan and Carpenter for plates, although our measured values of virtual mass and drag coefficients appear to be somewhat lower than values extrapolated from their data (for plates).

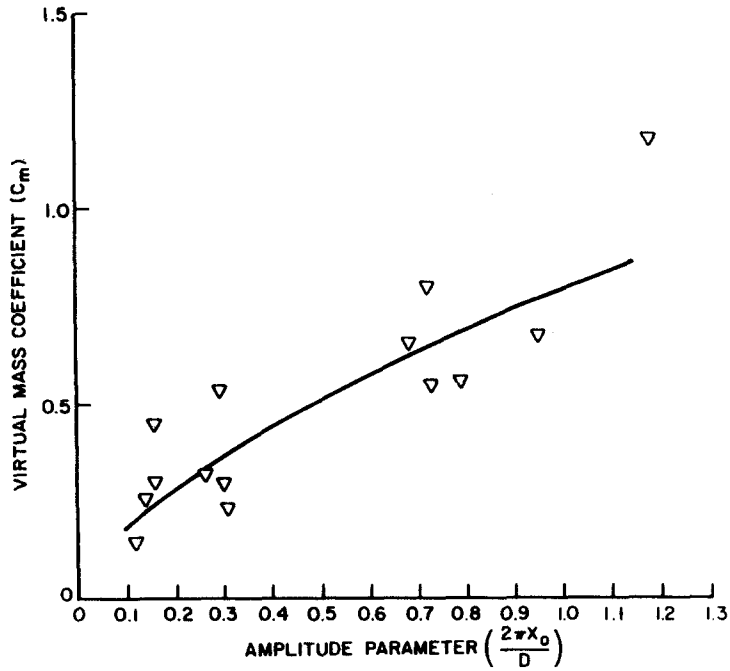

Figure 16. Variation of virtual mass coefficient with amplitude parameter for a void fraction of 19%.

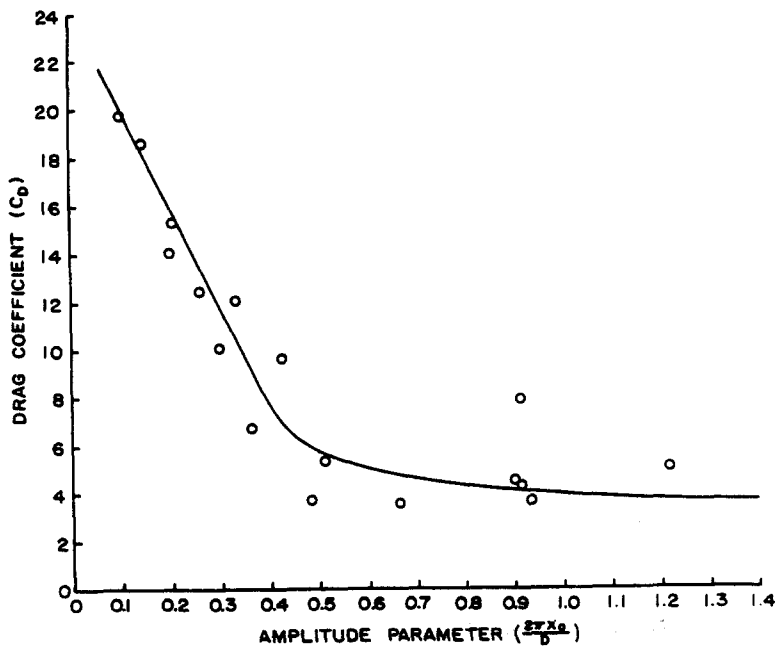

Figure 17. Variation of drag coefficient with amplitude parameter for single-phase liquid ($\langle\alpha\rangle = 0$).

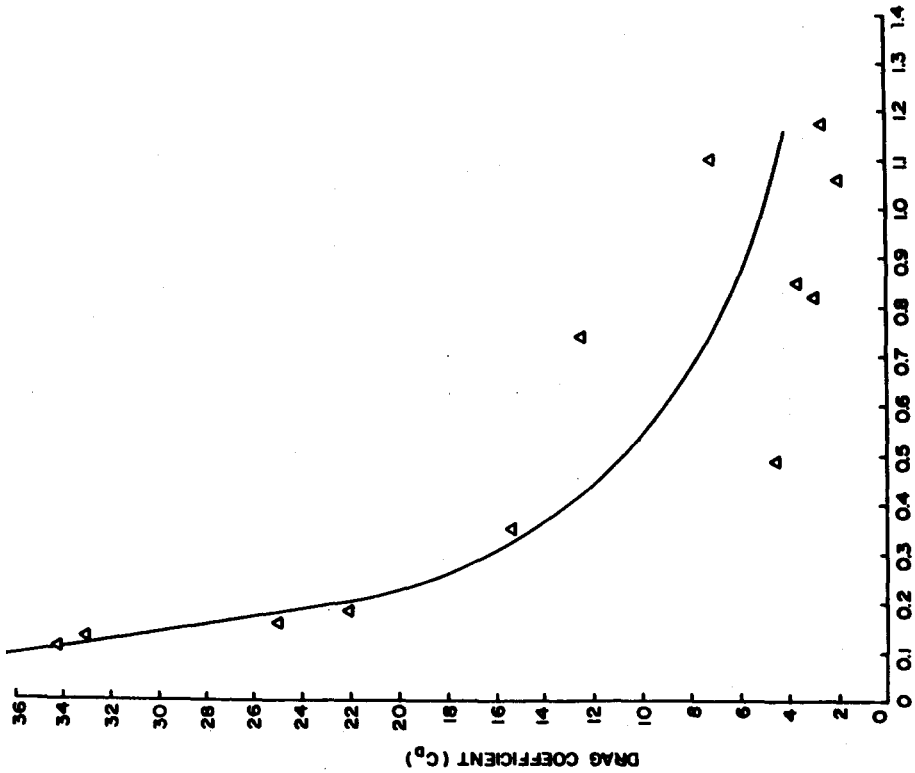

Figure 19. Variation of drag coefficient with amplitude parameter for a void fraction of 7%.

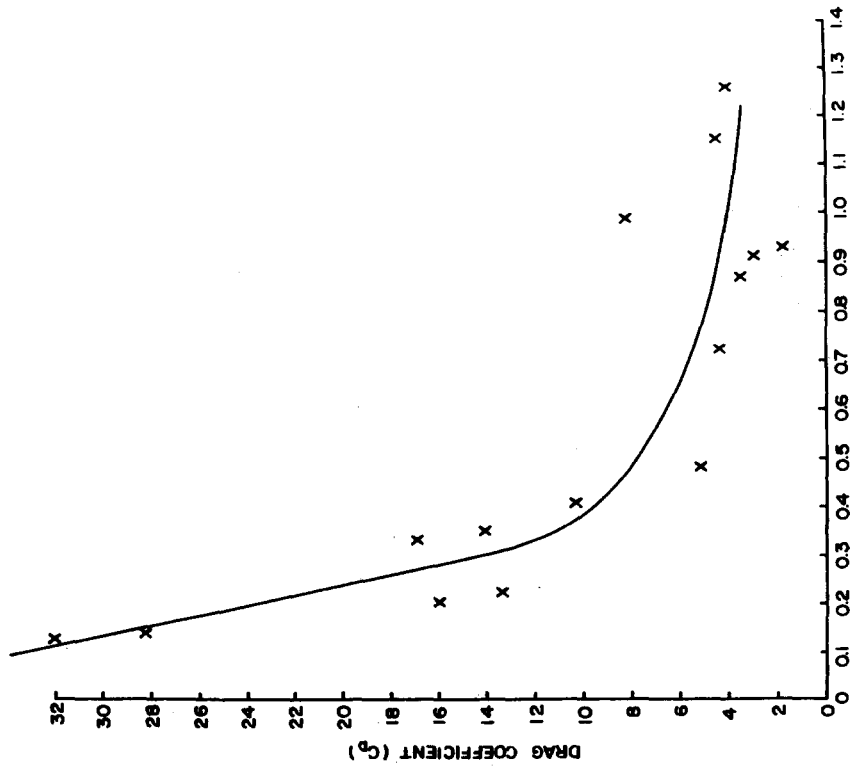

Figure 18. Variation of drag coefficient with amplitude parameter for a void fraction of 3.5%.

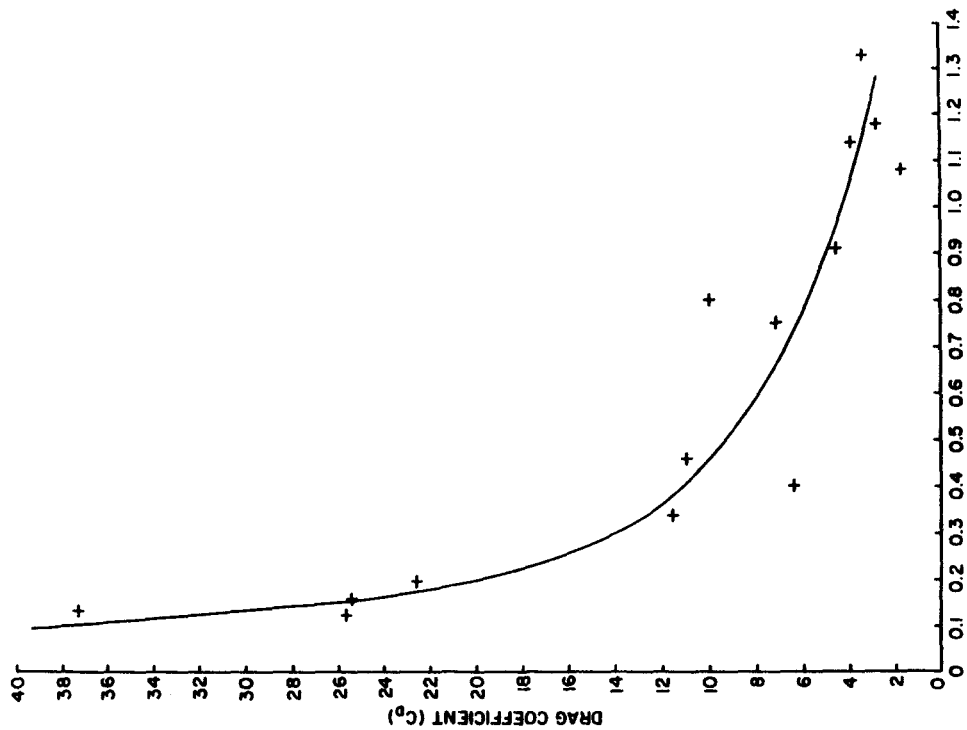

Figure 21. Variation of drag coefficient with amplitude parameter for a void fraction of 15.5%.

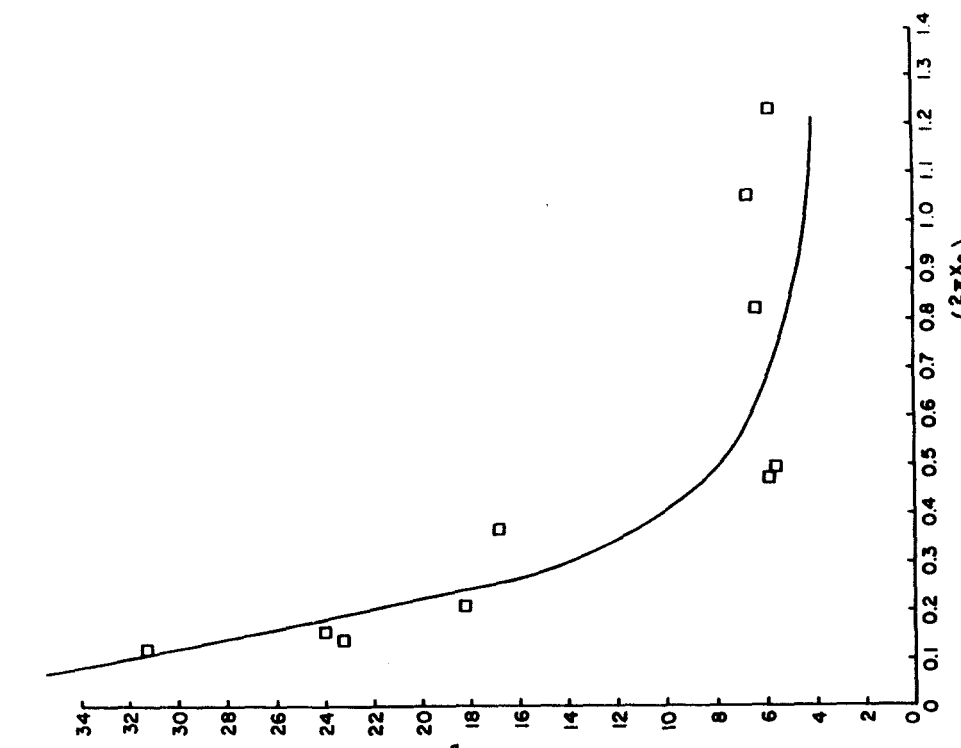

Figure 20. Variation of drag coefficient with amplitude parameter for a void fraction of 12%.

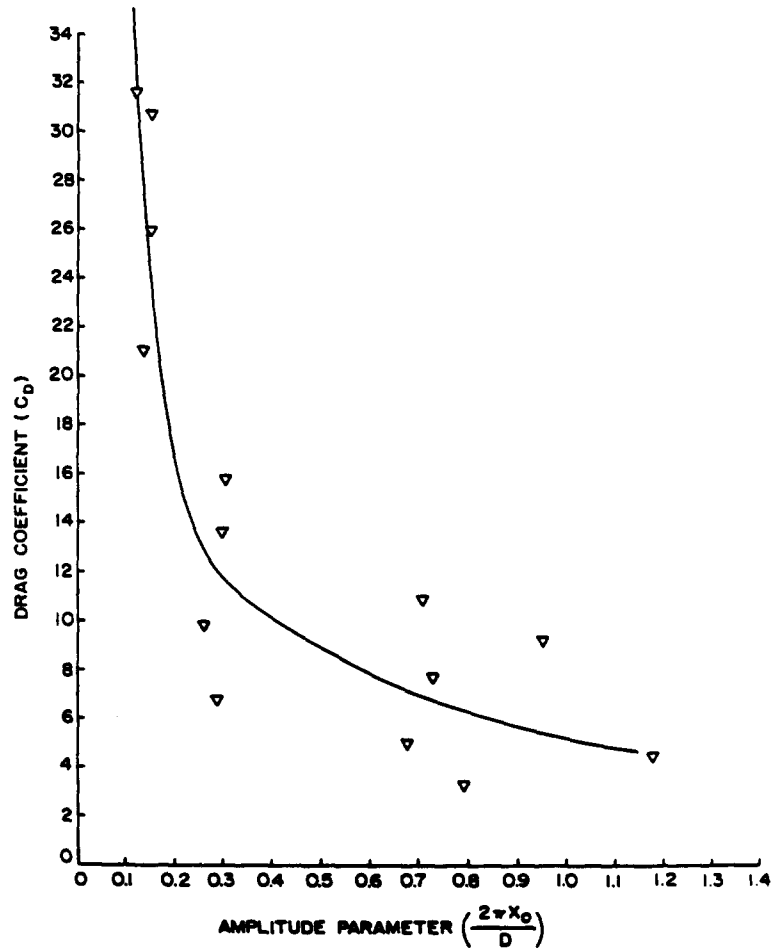

Figure 22. Variation of drag coefficient with amplitude parameter for a void fraction of 19%.

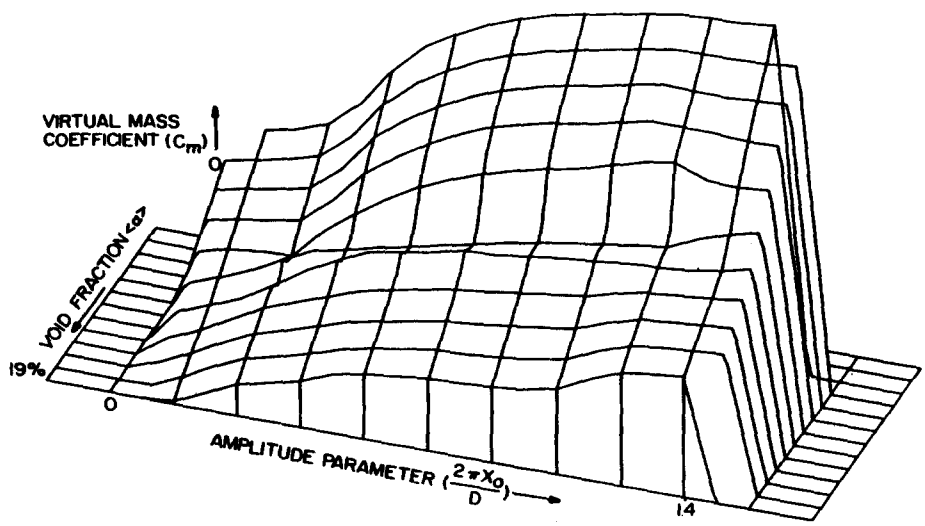

Figure 23. Three-dimensional plot of the virtual mass coefficient.

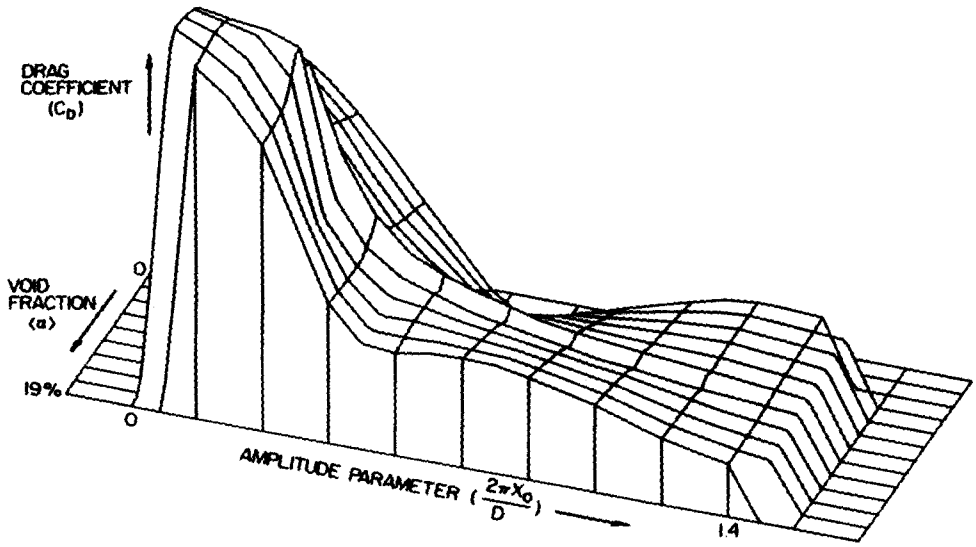

Figure 24. Three-dimensional plot of the drag coefficient.

As can be seen in figures 12–16 and figures 18–22 in a two-phase fluid, for the same value of the amplitude parameter, the virtual mass coefficients tend to become smaller, and the drag coefficients larger, with increasing void fractions. This trend can be seen more clearly in the three dimensional plots given in figures 23 and 24.

CONCLUSION

During a blowdown transient, the maximum amplitude parameter of an INEL drag-disk is expected to be of the order unity, since a drag-disk of diameter 0.763 cm (0.3 in.) experiences a maximum displacement of the order of 0.1 cm. For this amplitude parameter the experimentally determined virtual mass coefficient is of the order of unity. It has been shown previously by Kamath & Lahey (1980), that a virtual mass coefficient as large as 5.0 had a negligible effect on the transient response of the disk. Thus, we can conclude that the effect of the virtual mass of the disk is negligible in the transient analysis of the INEL drag-disk, both in single and two-phase flows.

NOMENCLATURE

A_0 amplitude of sinusoidal acceleration
C_D drag coefficient
C_m virtual mass coefficient
D diameter of the disk
E Young's modulus of the material of the beam
f frequency
f_c cutoff frequency of the numerical filter
f_n natural frequency of disk and beam
f_0 frequency of Oscillation
f_s sampling frequency
f_T roll-off termination frequency of the numerical filter
F_d drag force on disk
F_{vm} virtual mass force on disk
G mass flux
g_c gravitational constant

h thickness of the beam
I second moment of the area of the cross-section of a beam about its neutral axis
j square root of -1
k spring constant
l length of the beam
L equivalent length, $l + D/2$
M mass of disk and beam
N number of data samples in one run
p pressure
t time
T_0 half the time period of one run
U_m center-of-mass velocity
u_0 amplitude of sinusoidal velocity
v_k velocity of phase-k
x displacement of the disk
$\dot{x}$ velocity of the disk
$\ddot{x}$ acceleration of the disk
$\bar{x}$ exponential Fourier Transform of x
$\bar{x}^*$ complex conjugate of $\bar{x}$
x_0 amplitude of the (sinusoidal) displacement

Greek symbols

α void fraction
Δt time internal between samples
$\bar{\rho}$ two-phase density, $\rho_l(1 - \langle\alpha\rangle) + \rho_v\langle\alpha\rangle$
ρ_k density of phase-k ($k = l$ or "v")
μ_k dynamic viscosity of phase-k ($k = l$, or v)
$\mu_{2\phi}$ dynamic viscosity of the two-phase mixture, $\mu_l(1 - \langle\alpha\rangle) + \mu_v\langle\alpha\rangle$
ω angular frequency
$\langle\xi\rangle$ cross-sectional average of ξ
$\triangleq$ is defined by
y^* complex conjugate of y

REFERENCES

BRIGHAM, O. E. 1974 *The Fast Fourier Transform*. Prentice-Hall, Englewood Cliffs, New Jersey.

CARBODY, T. 1964 Establishment of the wake behind a disk. *J. Basic Engng* **86**, 869–882.

GARRISON, C. J., FIELD, J. B. & MAY, M. D. 1977 Drag and inertial forces on a cylinder in periodic flow. *J. of the Waterway Port Coastal and Ocean Div.* **103**, N. WW2.

KAMATH, P. S. & LAHEY, R. T., JR. 1981 Transient analysis of DTT rakes. *NUREG/CR*-2151.

KAMATH, P. S. & LAHEY, R. T., JR. 1980 A turbine-meter evaluation model for two-phase transients. *J. Heat Transfer* **102**.

KEULEGAN, G. H. & CARPENTER, L. H. 1958 Forces on cylinders and plates in an oscillating fluid. *J. of Research of the National Bureau of Standards* **60**, 423–440.

LAI, R. Y. S. 1973 Translatory accelerating motion of a circular disk in a viscous fluid. *Appl. Sci. Res.* **27**.

LYLE, F. M. & LAI R. Y. S. 1972 The Stokes-flow drag on prolate and oblate spheroids during axial translatory acceleration. *J. Fluid Mech.* **52**.

MERCIER J. A. 1973 Large amplitude oscillations of a circular cylinder in a low-speed steam. Ph.D. Dissertation, Stevens Institute of Technology.

MORRISON, J. R., *et al.* 1950 The force exerted by surface waves on piles. *Petroleum Trans.* **189**, 149–157.

ORMSBY, J. F. A. 1971 Design of numerical filters with applications to missile data processing. *J. Assoc. Comput. Mach.* **18**, 440–466.

SARPKAYA, T. 1975 Forces on cylinders and spheres in a sinusoidally oscillating fluid. *J. Appl. Mech.* **42**, 32–37.